Nanoscale imaging of equilibrium quantum Hall edge currents and of the magnetic monopole response in graphene

Aviram Uri [1]*, Youngwook Kim[2,3], Kousik Bagani[1], Cyprian K. Lewandowski[4], Sameer Grover[1], Nadav Auerbach[1], Ella O. Lachman[1,6], Yuri Myasoedov[1], Takashi Taniguchi[5], Kenji Watanabe[5], Jurgen Smet[2] and Eli Zeldov[1]*

Although the recently predicted topological magnetoelectric effect[1] and the response to an electric charge that mimics an induced mirror magnetic monopole[2] are fundamental attributes of topological states of matter with broken time-reversal symmetry, so far they have not been directly observed in experiments. Using a SQUID-on-tip[3], acting simultaneously as a tunable scanning electric charge and as an ultrasensitive nanoscale magnetometer, we induce and directly image the microscopic currents generating the magnetic monopole response in a graphene quantum Hall electron system. We find a rich and complex nonlinear behaviour, governed by the coexistence of topological and non-topological equilibrium currents, that is not captured by the monopole models[2]. Furthermore, by imaging the equilibrium currents of individual quantum Hall edge states, we reveal that the edge states, which are commonly assumed to carry only a chiral downstream current, in fact carry a pair of counterpropagating currents[4], in which the topological downstream current in the incompressible region is counterbalanced by a non-topological upstream current flowing in the adjacent compressible region. The intricate patterns of the counterpropagating equilibrium-state orbital currents provide insights into the microscopic origins of the topological and non-topological charge and energy flow in quantum Hall systems.

Magnetic monopole is a hypothetical elementary particle representing an isolated source of magnetic field with only one magnetic pole (N without S, or vice versa) and a quantized magnetic charge. Although modern particle theory predicts its existence, experimental searches for magnetic monopoles have so far been unsuccessful. Condensed matter systems, however, offer a natural platform for studying magnetic monopole-like excitations or response in materials like spin ice[5,6] or topological insulators owing to their topological magnetoelectric effect (TME)[1,7,8]. The conventional magnetoelectric effect (ME) describes magnetization induced by an externally applied electric field in materials in which the time-reversal symmetry is broken either by magnetic order or by an applied magnetic field[9]. This non-topological ME is distinctly local in nature—the local magnetization $\mathbf{m}$ is proportional to the local electric field $\mathbf{E}$ through $m_i = \alpha_{ij}E_j$, where α_{ij} is the so-called Lifshitz tensor[9]. In recent decades this ME has enabled key advances in

spin-based information processing and has been exploited in fast-access magnetic memory, which is of keen practical interest[10].

The advent of topology has led to the notion that topological systems can exhibit a magnetoelectric effect of an entirely different nature with two fundamentally different characteristics—nonlocality and the topologically quantized response[1,7,8]. This TME is predicted to arise in three-dimensional (3D) magnetic topological insulators and in 2D electron systems with quantized Hall conductivity. In these systems, topological currents may flow in the ground state. They are expected to generate an exotic response in the form of a mirror magnetic monopole characterized by the Chern number, C (refs. [2,11,12]). One can depict this TME by considering a point charge Q_e placed at $r = 0$ and height z_0 above the topological surface (Fig. 1a). In this case, the induced circulating topological surface current density

$$J_\varphi^T(r) = \frac{r\hat{\varphi}}{2\pi(r^2 + z_0^2)^{3/2}} Q_m'$$ (1)

produces a magnetic field, above the topological plane, equivalent to that of a mirror magnetic monopole positioned at a mirror-symmetric point with a universal value of induced magnetic charge of $Q_m' = C\alpha c Q_e$ (ref. [2]). Here $\alpha \approx 1/137$ is the fine-structure constant and c is the speed of light. Note that this response has been termed the magnetic monopole[2], even though Q_m' is not a real monopole because the induced magnetic field in Fig. 1a is pointing outwards above the plane and inwards below the plane such that $\nabla \cdot \mathbf{B} = 0$. Nonetheless, the magnetic monopole-like response has unique properties reflecting its topological nature that are fundamentally different from a conventional magnetic response. In particular, the induced local magnetization $m_z(r)$, found from the relation $\mathbf{J}^T = \nabla \times m_z\hat{z}$, is proportional to the local electric potential V, $m_z(r) = \sigma_{yx}V(r)$, which represents a non-local relation between surface magnetization and electric field $\mathbf{E}(r) = -\nabla V(r)$, which has no counterpart in non-topological systems. Here $\sigma_{yx} = Ce^2/h$ is the quantum Hall (QH) conductance, e is the elementary charge and h is Planck's constant. A striking manifestation of this non-locality is that the total magnetic moment induced by the point electric charge, $M = \int_0^\infty m_z(r)\,\mathrm{d}^2r = \int_0^\infty J_\varphi^T(r)\,r^2\,\mathrm{d}r$, as predicted from
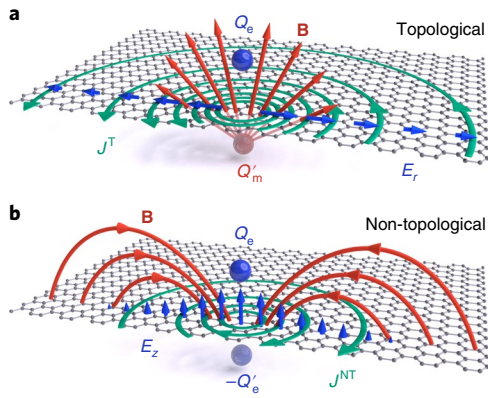
Fig. 1 | Magnetic monopole response and the topological and non-topological magnetoelectric effects. a, Schematic of an electric point charge Q_e (blue) creating an in-plane radial electric field E_r (blue arrows) in an incompressible QH ground state of a graphene monolayer. The TME gives rise to circulating topological currents $J_\varphi^T(r) = \sigma_{yx} E_r(r)$ (green) that decay as $1/r^2$. These currents generate a magnetic field above the graphene (red arrows) of a mirror magnetic monopole with charge Q_m' (transparent red). **b**, The same configuration as in **a**, but in a compressible QH state in which Q_e induces a mirror electric charge $-Q_e'$ (transparent blue) and an out-of-plane electric field (blue arrows). Because in this case the in-plane electric field is screened ($E_r = 0$), one expects no circulating currents. Yet, counter-circulating non-topological currents J^{NT} (green) arise due to the non-topological ME generating an opposite magnetic field that corresponds to a magnetic dipole rather than a monopole.

equation (1), becomes infinite, a behaviour that is in sharp contrast to the conventional ME response. Remarkably, infinite magnetic moment also implies infinite energy $U = -\mathbf{M} \cdot \mathbf{B}$, which is required to generate the magnetic monopole response, which is cut off in reality by the proximity to the backgate, the system size and by disorder, as we show in the following. Here, $\mathbf{B} = B\hat{z}$ is the applied magnetic field.

The TME and the corresponding magnetic monopole response have so far eluded direct microscopic observation[11–14]. The technical challenges lie in the need to bring a controllable electric charge into close proximity to a topological surface and in measuring the resulting minute local magnetic response. We accomplished this by utilizing a nanoscale superconducting quantum interference device (SQUID) fabricated on the apex of a sharp pipette (SQUID-on-tip, SOT)[3]. Here, Pb SOTs have been deployed with a typical diameter of $d = 60$ nm and scanned at a height of $h \approx 30$ nm above the sample surface at $T = 300$ mK. They possess magnetic field sensitivity of 30 nT Hz$^{-1/2}$ and spin sensitivity of $0.5\,\mu_B$ Hz$^{-1/2}$ in a background applied magnetic field of $B \approx 1$ T (Methods section 'SOT fabrication and characterization').

Our topological system of choice is hexagonal boron nitride (hBN)-encapsulated graphene in the QH state (Methods sections 'Device fabrication' and 'Transport data' and Supplementary Figs. 1 and 2). Such van der Waals heterostructures have the advantage of exhibiting low disorder, large Landau level (LL) energy spacing, and well resolved QH states even at moderate B (refs. [15,16]). This system offers exceptional density tunability and the electronic states are in close proximity to the sample surface. With the help of backgates, p–n junctions can be formed and the Chern numbers can be tuned in situ[17,18]. This is not possible in magnetic topological insulators, which so far support only $C = \pm 1$ (refs. [19,20]).

We use three different strategies to create an electric charge and the corresponding spatially dependent electric fields to explore the various regimes of the ME. The first method exploits native disorder such as charged impurities and potential variations in the sample,

which induce a ME response that is spatially imaged with the SOT. This approach can provide essential information on the structure of the disorder but lacks controllability. The second method makes use of the creation of tunable local potential in a lateral p–n junction induced by two separate backgates[17,18]. We use it to directly image the microscopic equilibrium currents of the QH edge states. The third method is based on the application of a non-zero voltage V_{tg} to the SOT, creating controllable charge or potential at the tip apex and measuring the local ME response using the SOT.

We first discuss the TME arising due to native disorder, for example a point charge Q_e localized at the hBN top surface (Fig. 2a). This charge, located at $(0,0,z_0)$, generates a radial electric field in the graphene plane in the incompressible QH state, $E_r(r) = \frac{r}{4\pi\varepsilon(r^2 + z_0^2)^{3/2}} Q_e$ (ε is the effective permittivity), which in turn induces a circulating current $J_\varphi^T(r) = \sigma_{yx} E_r(r)$ (Methods section 'TME response to a point charge') and the corresponding mirror magnetic monopole Q_m' according to equation (1). The numerically calculated $J_\varphi^T(r)$ is presented in Fig. 2b versus the global filling factor ν, controlled by the backgate voltage V_{bg} (Methods section 'Semiclassical numerical simulations' and Supplementary Fig. 10). As expected, $J_\varphi^T(r)$ decays with r and is present only in the incompressible states with integer filling factors $\nu = C = \pm 2, \pm 6, \pm 10, \ldots$ when the Fermi level ϵ_F resides within the LL energy gaps. The magnitude of the current grows with the Chern number $|C|$ (as $\sim \sqrt{|C|}$; Supplementary Section 1) and is of opposite chirality for electrons ($C > 0$) and holes ($C < 0$). In the compressible metallic regime, in contrast, $E_r(r)$ is screened and hence the topological currents are eliminated entirely. Note that these topological currents are usually referred to as chiral QH edge state currents and are commonly assumed to be the only currents flowing in the system. However, as we show below, the equilibrium QH edge states, rather than carrying these downstream currents along the chirality direction, carry pairs of counterpropagating downstream and upstream currents. These currents originate from two different mechanisms pertaining to the topological and non-topological MEs, respectively, and we will refer to them as J^T and J^{NT}, respectively. Note that in the literature these currents are vaguely termed 'bulk current' and 'edge current', respectively[4].

To detect the microscopic currents, we attach the SOT to a quartz tuning fork (TF) and oscillate the SOT parallel to the graphene surface with a small amplitude x_{ac} along the $\hat{x}$ direction (Fig. 2a and Methods section 'Tuning fork'). The SOT thus measures the corresponding $B_z^{TF}(x,y) = x_{ac} \partial B_z(x,y)/\partial x \propto J_y(x,y)$ (Fig. 2h) and provides a direct visualization of the y component of the local current $J_y(x,y)$ (Methods section 'Modulation techniques' and Supplementary Fig. 3). Figure 2i shows profiles of $B_z^{TF}(x)$ on sweeping V_{bg} through the compressible and incompressible QH states. At integer filling factors $\nu = C$, the data provide a direct local observation of the TME and a unique nanoscale rendering of the equilibrium topological currents. The observed behaviour is in good qualitative agreement with the described model (Fig. 2b), displaying $J_y^T(x) = \sigma_{yx} E_x(x)$ of varying sign with x, which grows with $|C|$ and changes the overall sign on crossing the zeroth LL.

Strikingly, in addition to the topological currents in the incompressible states, large currents are also observed in Fig. 2i in partially filled LLs, as further exemplified in the 2D image in Fig. 2h. Naively, no currents are expected in this compressible, metallic regime, due to screening of the in-plane electric field. Surprisingly, these currents are of opposite polarity to those in the incompressible state (see the colour inversion) and of comparable amplitude. Note that partial screening of the electric field due to finite compressibility will result in weaker currents, and cannot explain the observed polarity inversion, because the polarity of σ_{yx} and the direction of the external electric field will not change. We now show that these observed equilibrium currents are of an entirely different nature than the topological currents[4] and manifest a non-topological ME.
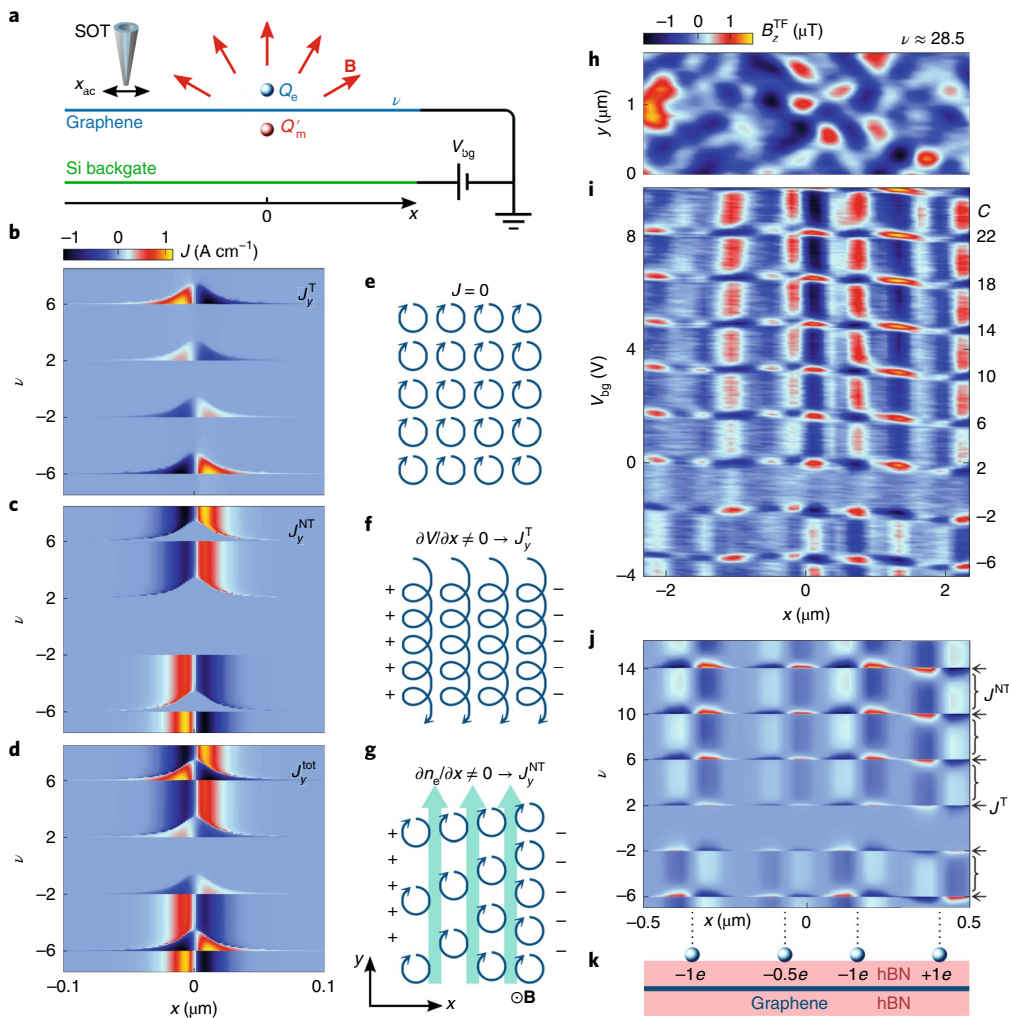
Fig. 2 | Topological and non-topological equilibrium currents in graphene in the presence of charge disorder. a, Schematic set-up showing an impurity charge Q_e (blue) inducing a response magnetic field B (red) in a form of mirror magnetic monopole Q'_m in the incompressible state. The backgate voltage V_{bg} controls the graphene global filling factor ν. **b**, Numerical simulation of $J^T_\varphi(r)$ versus global ν for a charge $Q_e = -0.5e$ positioned on top of the hBN surface 15 nm above the graphene. The plot shows the cross-section of $J^T_y(x)$ through the origin. **c**, Same as in **b** but for $J^{NT}_\varphi(r)$, which flows only in the compressible states with opposite chirality. **d**, The total current $J_\varphi = J^T_\varphi + J^{NT}_\varphi$. **e**, Semiclassical picture of cyclotron orbits of holes with mutually cancelling neighbouring currents resulting in zero total current. **f**, In the presence of an in-plane electric field E_x (indicated by + and − signs), the cyclotron orbits acquire a drift velocity resulting in a non-zero J^T_y in the incompressible state. **g**, In the compressible regime, the external in-plane electric field is screened by establishing a charge density gradient, giving rise to J^{NT}_y flowing in the opposite direction (cyan arrows). **h**, Experimental $B^{TF}_z(x, y) \propto J_y(x, y)$ for $\nu \approx 28.5$ compressible state, revealing equilibrium J^{NT} due to native charge disorder. The colour bar in **h** applies to **h–j**. **i**, Experimental $B^{TF}_z(x) \propto J_y(x)$ versus V_{bg}, revealing alternating bands of J^T and J^{NT} due to native disorder. Right axis labels indicate the corresponding bulk values of C. **j**, Numerically calculated $B^{TF}_z(x)$ versus ν induced by the four charges in **k**. Curly brackets and arrows indicate bands of J^{NT} and J^T, respectively. **k**, Illustration of the four impurity charges on the hBN surface used for calculations in **j**. For parameters, see Methods section 'Measurement and simulation parameters' and Source data.

These J^{NT} currents apparently do not couple directly to transport measurements[21] and, moreover, because they do not arise from the relation $\mathbf{J} = \sigma\mathbf{E}$, they are invisible to scanning probe techniques that do not measure currents directly, such as the Kelvin probe[22], scanning single-electron transistor[23] and scanning capacitance[24]. As a result, even though their existence was predicted theoretically[4], these currents have remained undetected so far. Our scanning SQUID-on-tip technique allows direct nanoscale imaging of these equilibrium currents.

The following semiclassical picture is instructive to distinguish the origin of the non-topological and topological currents (Supplementary Section 1). In strong magnetic fields and in the absence of an in-plane electric field, the electron or hole cyclotron

orbits can be described semiclassically as an array of circles resulting in zero average current (Fig. 2e). In the incompressible state, an in-plane electric field along the x direction, $E_x = -\partial V/\partial x$, causes the orbitals to convert into spirals drifting along the y direction and generating the current $J^T_y = \sigma_{yx} E_x$, as shown schematically in Fig. 2f. The topological nature of these equilibrium currents manifests itself in the fact that σ_{yx} is quantized. On the other hand, in the compressible regime, carriers redistribute themselves and screen the in-plane electric field. As a result J^T_y vanishes, but at a cost of a non-zero gradient in carrier density, $\partial n_e/\partial x$ (Fig. 2g). Because each orbital carries a magnetic moment[25], $\mu_e = -v_F\sqrt{|e\hbar n/2B|}\,\hat{z}$, which results in local magnetization $\mathbf{m} = |n_e|\mu_e$ (v_F being the Fermi velocity and n the LL index), the induced $\partial n_e/\partial x$ causes gradients in $\mathbf{m}$, and hence

produces equilibrium currents through[4] $\mathbf{J}^{NT} = \nabla \times \mathbf{m}$. This accounts for a non-zero $J_y^{NT} = \mu_e \partial |n_e|/\partial x$ in Fig. 2g, which flows in the direction opposite to the topological current J_y^T in Fig. 2f. Alternatively, J_y^{NT} can be understood as arising from uncompensated contributions to the current from neighbouring orbitals in the presence of a gradient in the orbital density (Fig. 2g). The J^{NT}s resemble magnetization currents in magnetic materials. Note, however, that here they do not arise as a diamagnetic or paramagnetic response to an applied magnetic field but rather as a non-topological magnetoelectric response to an applied electric field and hence can be of either polarity and of controllable magnitude. The corresponding quantum mechanical origins of both J^T and J^{NT} are described in Supplementary Section 1, with J^{NT} arising from the non-homogeneous distribution of the expectation value of the quantum mechanical current operator $\langle \hat{J}(x) \rangle$ (Supplementary Fig. 4). Figure 2c depicts J^{NT} generated by the point charge configuration of Fig. 2a, while the total current, $J^{tot} = J^T + J^{NT}$, is plotted in Fig. 2d. Figure 2j presents an example of calculated $B_z^{TF}(x)$ along a line crossing four point charges (Fig. 2k and Supplementary Fig. 10a), showing the evolution of alternating J^T and J^{NT} stripes, in qualitative agreement with the experimental data in Fig. 2i.

The topological and non-topological magnetoelectric effects in the QH regime display a remarkable duality (Fig. 1). An external charge Q_e induces a mirror electric charge $-Q_e'$ in a compressible state (Fig. 1b) and a mirror magnetic charge $Q_m' = C\alpha c Q_e$ in the incompressible phase (Fig. 1a). Both types of mirror charge give rise to circulating currents: $J^{NT}(r)$ originates from an out-of-plane component of the electric field $E_z(r)$ that determines $n_e(r)$ and $\nabla n_e(r)$, while J^T stems from the in-plane component $E_r(r)$. However, the two types of current are fundamentally different. In the non-topological case the magnetoelectric response to the charge Q_e induces currents that decay as $J^{NT}(r) \propto r^{-4}$, generating a total magnetic moment

$$M^{NT} = \pi \int_0^\infty J^{NT}(r) r^2 \mathrm{d}r = -Q_e \mu_e/e,$$ which is finite and local in

nature. In contrast, the topological response creates $J^T(r) \propto r^{-2}$, resulting in infinite magnetization M^T for any electric charge Q_e. This non-local diverging response is the hallmark of a topological phase with a broken time-reversal symmetry and accounts for the appearance of a mirror magnetic monopole rather than a magnetic dipole. Depending on the parameters, J^T and J^{NT} may become comparable (Supplementary Section 1 and Supplementary Fig. 5), but they are always of opposite chirality, as shown in the numerical simulations (Fig. 2b–d,j) and clearly observed in the experimental data in Fig. 2i. As V_{bg} is varied, the measured patterns in the adjacent compressible and incompressible bands have comparable magnitude but are of opposite sign, and the overall magnitude of J^T and J^{NT} grows with n (Supplementary Section 1). Remarkably, the zeroth LL shows essentially no non-topological J^{NT} in Fig. 2i, as indeed predicted theoretically (Supplementary Section 1 and Fig. 2c,j).

Rather than relying on the static native disorder, we can create a variable potential by adding a graphite backgate V_{bg}^L to the left half of the sample (Fig. 3a). By varying V_{bg}^L and the Si backgate V_{bg}^R, we can create a p–n junction with a tunable in-plane electric field E_x. Due to the charge density gradient, alternating compressible and incompressible stripes should thus be formed across the junction[4,22,26]. Utilizing this setting, we present here direct nanoscale imaging of the equilibrium currents in the QH edge states. Figure 3b–e shows a sequence of images of $B_z^{TF}(x,y) \propto J_y(x,y)$ as the filling factors ν_L and ν_R are increased with opposite polarities by sweeping V_{bg}^L and V_{bg}^R (see Supplementary Section 2 and Supplementary Video 1 for the full sequence). For $|\nu_L|, |\nu_R| < 2$, both sides of the junction are in the $n = 0$ LL (Fig. 3b) and no edge currents are present (in contrast to higher LLs; Supplementary Fig. 6). Once the $n = \pm 1$ LLs are reached, an incompressible strip carrying topological current I^T is formed on each side. The two incompressible strips carry I^T in

opposite directions, following the downstream chirality of the QH edge states as expected (blue arrows, Fig. 3c). As the potential difference across the junction is increased they move towards the centre. The remarkable observation, however, is that, as ν_L and ν_R are further increased, counterpropagating currents adjacent to I^T are formed (red arrows, Fig. 3d). These currents, which flow upstream against the QH chirality, are the result of the non-topological magnetoelectric contribution and are commonly ignored. This pair of counterpropagating equilibrium currents, I^T and I^{NT}, nearly cancel each other, so that the total edge current does not grow with further addition of LLs but merely oscillates (Fig. 3e). This mixed topological and non-topological magnetoelectric behaviour is more clearly resolved by inspecting line cuts across the junction (Fig. 3f), which show a tree-like pattern of I^T and I^{NT} pairs moving towards the centre with increasing filling factor difference across the junction, in agreement with the numerical simulations in Fig. 3g–j. Previous scanning probe studies could differentiate between compressible and incompressible regions[22,24,27,28], but the presence of I^{NT} was never uncovered.

By depleting carriers in the left side of the sample ($\nu_L = 0$) we can form fully controllable electrostatically defined QH edge states. This allows us to directly image the evolution of I^T and I^{NT} within individual QH edge states by varying V_{bg}^R, as presented in Methods section 'Electrostatically defined QH edge states', Supplementary Fig. 7 and Supplementary Video 2. Edge states in the context of transport studies are usually considered to be formed when a fully occupied LL with a gap above it crosses the Fermi level. This happens on approaching the sample edge where the carrier density is gradually depleted to zero (Supplementary Fig. 7g). Each edge state consists of an incompressible region with varying electric potential carrying downstream I^T followed by a compressible strip with constant electric potential that carries an upstream I^{NT}. Thus, in contrast to the common notion, each QH edge state under equilibrium conditions carries a pair of counterpropagating currents of comparable magnitude (Supplementary Section 1 and Supplementary Fig. 7g). In presence of an external bias, the global out-of-equilibrium transport current is carried by the overall net I^T, while the net I^{NT} should remain zero (Methods section 'Electrostatically defined QH edge states'). Locally, however, we expect the external bias to change the magnitude and the distribution of both J^T and J^{NT} within the individual QH edge states. This non-equilibrium change in the balance between the two counterpropagating currents provides important insight into the microscopic structure and dynamics of the QH edge states and may provide means (Methods section 'Electrostatically defined QH edge states') for local microscopic visualization of out-of-equilibrium processes of edge reconstruction and energy equilibration in integer and fractional QH states.

Employing the gained insight into the structure of the edge states we now address the general case of the monopole-like response induced by a variable charge or potential V_{tg} applied to the SOT (Fig. 4a). To generate a mirror magnetic monopole response, the entire sample has to be in an incompressible state. Hence, the potential drop along the graphene between the SOT location and far away, $\Delta V = V_0 - V_\infty = Q_e/4\pi \varepsilon z_0$, where z_0 is the height of the tip above the graphene surface, should not exceed the energy gap between the LLs, $e\Delta V_{max} = \Delta E_n = E_{n+1} - E_n$, where $E_n = \text{sign}(n)\sqrt{2e\hbar v_F^2|Bn|}$. This requirement imposes an upper bound on the allowable Q_e on the tip, equal to $Q_{max}^T = 4\pi \varepsilon z_0 \Delta E_n/e$. Equivalently, for the non-topological magnetoelectric effect, the maximum induced charge density variation should not surpass the density of states of a single LL, resulting in $Q_{max}^{NT} = 8\pi Be^2 z_0^2/h$. Remarkably, for our experimental configuration, Q_{max}^T and Q_{max}^{NT} are both of the order of just a single electron charge e (Methods section 'Monopole fragility' and Supplementary Fig. 8). When Q_e exceeds this value, the linear topological and non-topological magnetoelectric effects break down, giving rise to a regime where both effects are mixed. This mixed magnetoelectric
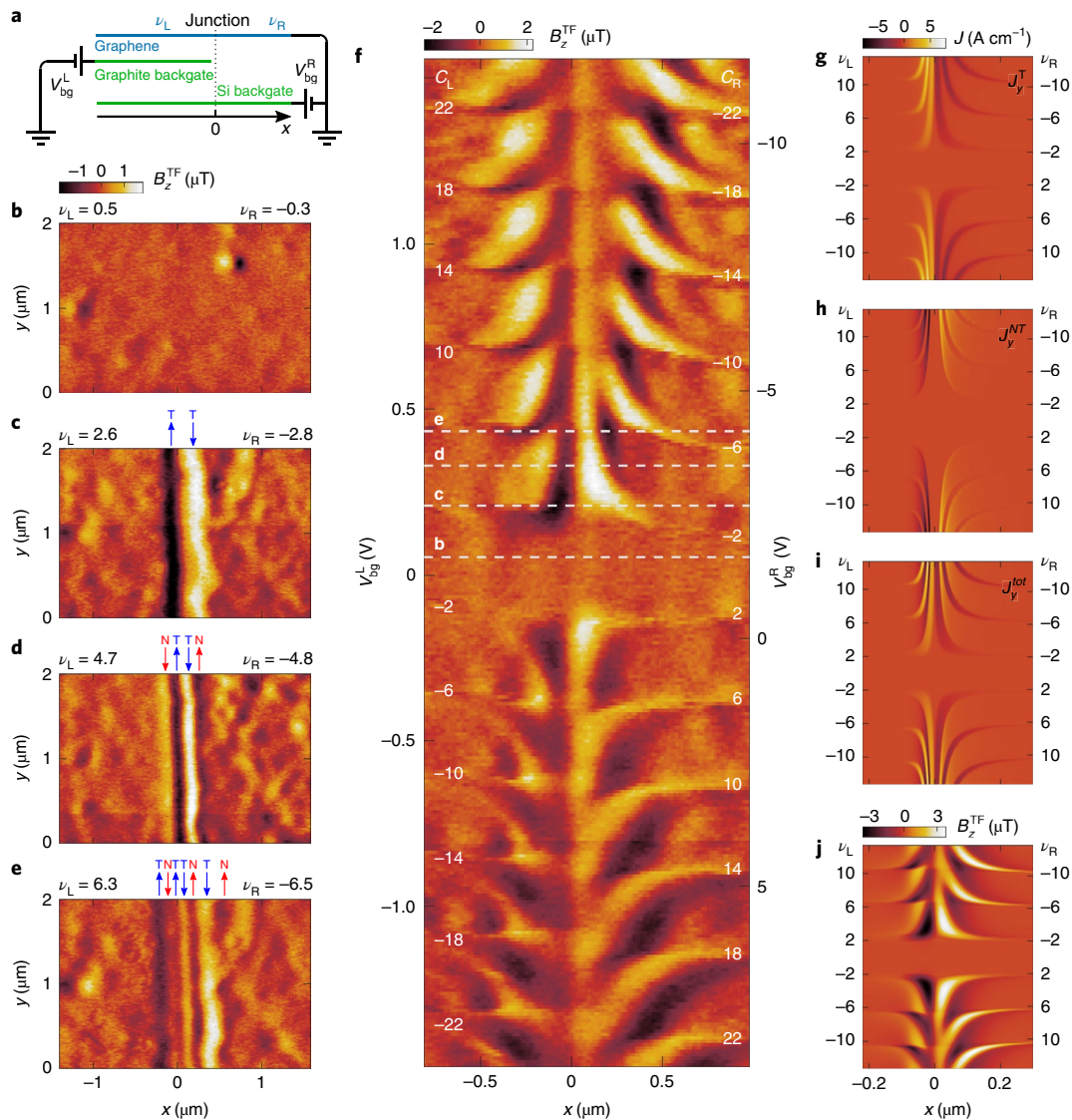
Fig. 3 | Topological and non-topological QH edge state currents in a p–n junction. a, Measurement set-up with graphite and Si backgates allowing independent tuning of the left and right filling factors ν_L and ν_R. **b–e**, 2D imaging of $B_z^{TF} \propto J_y$ of a graphene p–n junction at different filling factors ν_L and ν_R. Blue and red arrows mark I^T and I^{NT}, respectively, and their direction. **b**, In the zeroth LL, no currents are present along the junction. **c**, For $\nu_L = 2.6$ and $\nu_R = -2.8$, counterpropagating J^T current strips appear on the p and n sides of the junction (blue arrows). **d**, On increasing the density difference across the junction, the two J^T strips become closer, and subsequent strips with counterpropagating current J^{NT} emerge (red arrows). **e**, On further increasing the density difference, two additional J^T strips appear. **f**, Line scans across the junction sweeping V_{bg}^L and V_{bg}^R in opposite directions, revealing the spatial evolution of J^T and J^{NT}. Dashed lines mark the gate voltages at which the images in **b–e** were recorded. **g–j**, Numerical simulations reproducing the measurement in **f**, showing the evolution of J^T (**g**), J^{NT} (**h**), total current (**i**) and the calculated B_z^{TF} (**j**). For parameters, see Methods section 'Measurement and simulation parameters' and Source data.

effect (MME) exhibits a nonlinear response and a rich phase diagram beyond the mirror magnetic monopole framework[2,12], which has not been explored so far.

Figure 4b presents the numerically calculated B_z signal at the SOT position versus V_{bg} and V_{tg} and reveals a complex mixed magnetoelectric phase diagram in the form of tiled diamonds. The widely searched for topological mirror magnetic monopole state[2,11–14] is present only at singular points at the vertices of the diamonds in Fig. 4b in the limit of $V_{tg} \to 0$ (Supplementary Section 3 and Supplementary Fig. 9). The remainder of the phase diagram is dominated by the MME phase, in which each diamond corresponds to a different state classified by two quantum numbers (n_1, n_2), describing the LL numbers at infinity and below the tip, respectively (Fig. 4c). The middle row of diamonds with $n_1 = n_2$ describes the

non-topological magnetoelectric phase in which the entire sample is compressible. In the neighbouring diamonds with $n_2 = n_1 \pm 1$, the mixed magnetoelectric effect produces a response in the form of a magnetic dipole made up of a narrow ring of current I^T enclosed by counterpropagating current rings of I^{NT}, as illustrated in Fig. 4d–h. The following rows of diamonds originate from an increasing number of concentric rings of I^T and I^{NT} (Supplementary Fig. 9). Of particular interest are diamonds with $n_2 = -n_1$, corresponding to circular p–n junctions, where electron (hole) islands are formed in a hole (electron) doped sample. In this case concentric rings of I^T of opposite chirality appear, constituting magnetic quadrupole-like and higher order moments (Supplementary Fig. 9). The quantum mechanical calculation of the MME phase diagram (Supplementary Section 4) is presented in Supplementary Fig. 11 and shows good
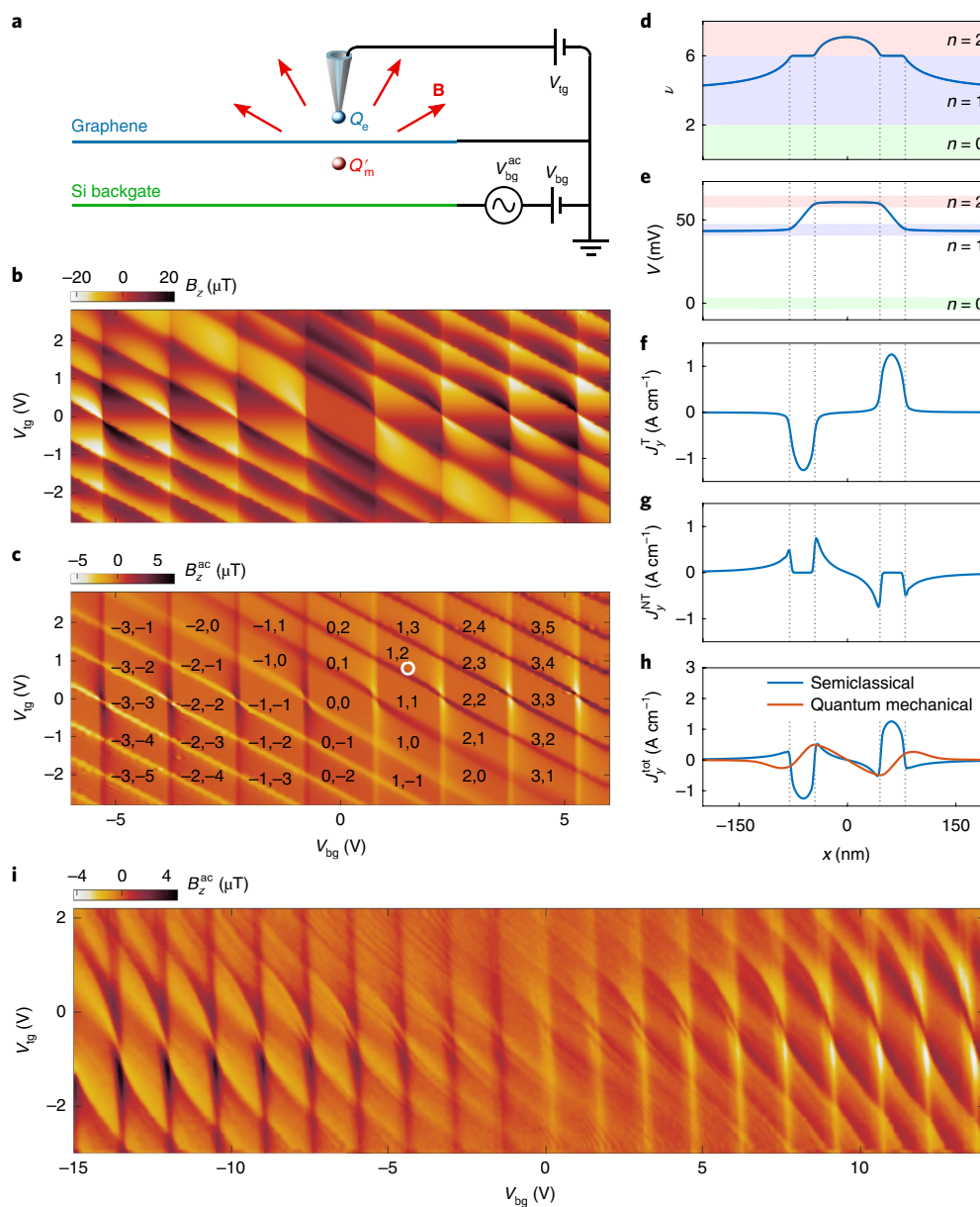
Fig. 4 | Mixed magnetoelectric effect. a, Schematic experimental set-up showing charge Q_e on the SOT inducing a mirror magnetic monopole Q'_m response. **b**, Numerical simulation of B_z at the location of the SOT versus V_{bg} and V_{tg}. **c**, Calculated B_z^{ac} in response to an a.c. excitation V_{bg}^{ac}, reproducing the experimental results in **i**. Diamonds are characterized by quantum numbers (n_1, n_2) indicating the LL far from the SOT and below it, respectively. The induced magnetic monopole response is present only at the vertices of the diamonds at $V_{tg} \approx 0$. **d–h**, Calculated filling factor ν (**d**), potential V (**e**), J^T in the incompressible regions (**f**), J^{NT} in the compressible regions (**g**) and the total current $J^{tot} = J^T + J^{NT}$ (**h**) versus position x with the SOT stationed at the origin, for $V_{bg} = 1.5$ V and $V_{tg} = 0.8$ V (white circle in **c**). **i**, Colour rendering of the experimentally measured B_z^{ac} in response to V_{bg}^{ac} versus V_{bg} and V_{tg}, revealing the rich phase diagram of the MME. For parameters, see Methods section 'Measurement and simulation parameters' and Source data.

general agreement with the semiclassical results. Figure 4h shows a comparison of J^{tot} calculated by both methods. The quantum mechanical QH wavefunction extending over a few magnetic lengths $l_B = \sqrt{\hbar/eB} \approx 25$ nm causes smoothing of the sharp current variations seen in the semiclassical calculation, emphasizing the common quantum mechanical origin of J^T and J^{NT} (Supplementary Fig. 12).

To increase the signal-to-noise ratio, rather than measuring B_z, we measure $B_z^{ac} = V_{bg}^{ac} \partial B_z / \partial V_{bg}$ by adding a small a.c. modulation V_{bg}^{ac} to V_{bg}, as illustrated in Fig. 4a (Methods section 'Modulation techniques'). The experimental data in Fig. 4i are in good agreement with the calculated B_z^{ac} in Fig. 4c, revealing the complex phase diagram of the MME (Supplementary Section 3). In addition, some fine structure in B_z^{ac} is resolved within the diamonds in Fig. 4i,

which can be ascribed to the bound electronic states within the tip-induced 'wedding cake' potential (Supplementary Section 4) recently observed in scanning tunnelling microscopy studies[29–31].

The presented direct nanoscale imaging of the equilibrium currents provides a new perspective on the microscopic nature of the current flow in the QH state that cannot be gained from global measurements. In particular, the QH edge states are shown to carry pairs of counterpropagating currents in the incompressible and compressible regions that are the manifestation of the topological and non-topological magnetoelectric effects. Rather than being present only along the sample edges, these currents can flow anywhere in the sample in response to potential variations induced either by externally applied gate voltages or by charge disorder

within the sample. This microscopic description lays the framework for comprehension of unconventional QH states that are expected to arise in more complex systems with intrinsic variations in the local chemical potential like magic angle twisted bilayer graphene[32], inhomogeneously or magnetically doped 2D topological insulators[33] or charged edge impurities[34]. Imaging equilibrium currents at the nanoscale has the potential to be used as a novel probe of the internal structure of the quantum mechanical currents and wavefunctions, and to shed light on the microscopic mechanisms of charge and heat transport in the QH edge states. The developed technique can be readily extended to imaging out-of-equilibrium currents for revealing transport mechanisms in quantum spin Hall, quantum anomalous Hall and equilibration processes in complex edge reconstruction structures in integer and fractional QH states.

Online content

Any methods, additional references, Nature Research reporting summaries, source data, extended data, supplementary information, acknowledgements, peer review information; details of author contributions and competing interests; and statements of data and code availability are available at https://doi.org/10.1038/s41567-019-0713-3.

References

1. Qi, X.-L., Hughes, T. L. & Zhang, S.-C. Topological field theory of time-reversal invariant insulators. *Phys. Rev. B* **78**, 195424 (2008).
2. Qi, X.-L., Li, R., Zang, J. & Zhang, S.-C. Inducing a magnetic monopole with topological surface states. *Science* **323**, 1184–1187 (2009).
3. Vasyukov, D. et al. A scanning superconducting quantum interference device with single electron spin sensitivity. *Nat. Nanotechnol.* **8**, 639–644 (2013).
4. Geller, M. R. & Vignale, G. Currents in the compressible and incompressible regions of the two-dimensional electron gas. *Phys. Rev. B* **50**, 11714–11722 (1994).
5. Bramwell, S. T. et al. Measurement of the charge and current of magnetic monopoles in spin ice. *Nature* **461**, 956–959 (2009).
6. Morris, D. J. P. et al. Dirac strings and magnetic monopoles in the spin ice $Dy_2Ti_2O_7$. *Science* **326**, 411–414 (2009).
7. Essin, A. M., Moore, J. E. & Vanderbilt, D. Magnetoelectric polarizability and axion electrodynamics in crystalline insulators. *Phys. Rev. Lett.* **102**, 146805 (2009).
8. Nomura, K. & Nagaosa, N. Surface-quantized anomalous Hall current and the magnetoelectric effect in magnetically disordered topological insulators. *Phys. Rev. Lett.* **106**, 166802 (2011).
9. Landau, L. D. & Lifshitz, E. M. *Electrodynamics of Continuous Media* (Pergamon, 1984).
10. Fusil, S., Garcia, V., Barthélémy, A. & Bibes, M. Magnetoelectric devices for spintronics. *Annu. Rev. Mater. Res.* **44**, 91–116 (2014).
11. Dziom, V. et al. Observation of the universal magnetoelectric effect in a 3D topological insulator. *Nat. Commun.* **8**, 15197 (2017).
12. Pesin, D. A. & MacDonald, A. H. Topological magnetoelectric effect decay. *Phys. Rev. Lett.* **111**, 016801 (2013).
13. Meier, Q. N. et al. Search for the magnetic monopole at a magnetoelectric surface. *Phys. Rev. X* **9**, 011011 (2019).
14. Xi, W. & Ku, W. Hunting down magnetic monopoles in two-dimensional topological insulators and superconductors. *Phys. Rev. B* **100**, 121201 (2018).
15. Dean, C. R. et al. Boron nitride substrates for high-quality graphene electronics. *Nat. Nanotechnol.* **5**, 722–726 (2010).
16. Mayorov, A. S. et al. Micrometer-scale ballistic transport in encapsulated graphene at room temperature. *Nano Lett.* **11**, 2396–2399 (2011).
17. Williams, J. R., DiCarlo, L. & Marcus, C. M. Quantum Hall effect in a gate-controlled p–n junction of graphene. *Science* **317**, 638–641 (2007).
18. Özyilmaz, B. et al. Electronic transport and quantum Hall effect in bipolar graphene p–n–p junctions. *Phys. Rev. Lett.* **99**, 166804 (2007).
19. Chang, C.-Z. et al. Experimental observation of the quantum anomalous Hall effect in a magnetic topological insulator. *Science* **340**, 167–170 (2013).
20. Mogi, M. et al. A magnetic heterostructure of topological insulators as a candidate for an axion insulator. *Nat. Mater.* **16**, 516–521 (2017).
21. Cooper, N. R., Halperin, B. I. & Ruzin, I. M. Thermoelectric response of an interacting two-dimensional electron gas in a quantizing magnetic field. *Phys. Rev. B* **55**, 2344–2359 (1997).
22. Weis, J. & von Klitzing, K. Metrology and microscopic picture of the integer quantum Hall effect. *Philos. Trans. R. Soc. A* **369**, 3954–3974 (2011).
23. Feldman, B. E., Krauss, B., Smet, J. H. & Yacoby, A. Unconventional sequence of fractional quantum Hall states in suspended graphene. *Science* **337**, 1196–1199 (2012).
24. Suddards, M. E., Baumgartner, A., Henini, M. & Mellor, C. J. Scanning capacitance imaging of compressible and incompressible quantum Hall effect edge strips. *New J. Phys.* **14**, 083015 (2012).
25. Kim, P. in *Dirac Matter* Vol. 71 (eds Duplantier, B., Rivasseau, V. & Fuchs J. N.) 1–23 (Springer, 2017).
26. Chklovskii, D. B., Shklovskii, B. I. & Glazman, L. I. Electrostatics of edge channels. *Phys. Rev. B* **46**, 4026–4034 (1992).
27. Cui, Y.-T. et al. Unconventional correlation between quantum Hall transport quantization and bulk state filling in gated graphene devices. *Phys. Rev. Lett.* **117**, 186601 (2016).
28. Lai, K. et al. Imaging of Coulomb-driven quantum Hall edge states. *Phys. Rev. Lett.* **107**, 176809 (2011).
29. Freitag, N. M. et al. Electrostatically confined monolayer graphene quantum dots with orbital and valley splittings. *Nano Lett.* **16**, 5798–5805 (2016).
30. Ghahari, F. et al. An on/off Berry phase switch in circular graphene resonators. *Science* **356**, 845–849 (2017).
31. Gutiérrez, C. et al. Interaction-driven quantum Hall wedding cake-like structures in graphene quantum dots. *Science* **361**, 789–794 (2018).
32. Uri, A. et al. Mapping the twist angle and unconventional Landau levels in magic angle graphene. Preprint at https://arxiv.org/abs/1908.04595 (2019).
33. Rosen, I. T. et al. Chiral transport along magnetic domain walls in the quantum anomalous Hall effect. *npj Quantum Mater.* **2**, 69 (2017).
34. Marguerite, A. et al. Imaging work and dissipation in the quantum Hall state in graphene. *Nature* **575**, 628–633 (2019).

Methods

Device fabrication. Three graphene-based van der Waals heterostructures were measured (Supplementary Fig. 1). All devices consisted of a hBN/graphene/hBN stack placed on top of a 300-nm-thick SiO$_2$ layer of a thermally oxidized doped silicon wafer, acting as a backgate. A graphitic layer was placed under part of the stack, serving as an additional backgate. The two backgates allowed us to induce an interface of two different filling factors, ν_L and ν_R, at the boundary of the graphitic layer (Fig. 3a). The van der Waals stacking of device A was carried out using the viscoelastic transfer method, as explained in ref. [35]. Devices B and C were created with the Elvacite-based pick-up method reported in refs. [35,36]. To minimize the SOT distance to the graphene, we used a relatively thin top hBN layer with a thickness of ~8 nm (devices A and C) or 11.5 nm (device B). The bottom hBN layer was 23 nm (device A) or 50 nm (devices B and C) thick. The graphite backgate layer had a thickness of ~5 nm. The heterostructures were annealed in an Ar/H$_2$ forming gas atmosphere at 500 °C to remove bubbles and wrinkles before further processing. Patterning was performed using electron beam lithography and etching as described in ref. [37]. Contacts and leads were fabricated by thermal evaporation of a 10-nm-thick Cr adhesion layer followed by a 50–70 nm Au layer. The SOT scanning studies require an exceptionally clean surface. To ensure this, extra cleaning steps were carried out. After liftoff, the devices were re-annealed at 350 °C. Contact mode atomic force microscopy was deployed to sweep off PMMA residues[38,39], at a scanning speed between 0.4 and 0.6 Hz and with a tip force between 50 and 150 nN, depending on the device shape and the residue height.

Transport data. Four-point transport measurements were performed using standard lock-in techniques with a bias current of $I = 100$ nA (r.m.s.) at 7 Hz. From low magnetic field data we calculated the mobility $\mu = \frac{1}{e n_e \rho_{xx}}$ and mean free path $l_{mfp} = \frac{1}{2 k_F \rho_{xx}} \frac{h}{e^2}$, where $n_e = \left[e \frac{d\rho_{xy}}{dB} \right]^{-1}$ is the carrier density, $\rho_{xx} = \frac{V_x}{I} \frac{W}{L}$ is the longitudinal four point resistivity, $\rho_{xy} = \frac{V_H}{I} \frac{W}{L}$ is the Hall resistivity, V_x and V_H are the longitudinal and transverse voltages, respectively, L and W are the length and width of the sample between the relevant transport contacts, respectively, and $k_F = \sqrt{\pi n_e}$ is the Fermi wavevector. Our devices showed a mean free path of l_{mfp} of 1–8 μm and mobility $\mu \approx 10^5 - 10^6$ cm^2 V^{-1} s^{-1} in the Si gated regions. The graphite gated regions displayed a lower mobility of $\mu \approx 10^4 - 10^5$ cm^2 V^{-1} s^{-1} and l_{mfp} of 0.05–1 μm. Supplementary Fig. 2 shows a Landau fan diagram of device C in the Si gated region.

SOT fabrication and characterization. The Pb SOTs were fabricated as described in ref. [3] with diameters ranging from 50 to 80 nm and including an integrated shunt resistor on the tip[40,41]. Magnetic imaging was performed in a ^{3}He system[42,43] at 300 mK, at which the Pb SOTs can operate in magnetic fields up to 1.8 T, directed along $\hat{z}$, perpendicular to the SQUID loop. At the fields of $B \approx 1$ T used in this study, the SOTs displayed flux noise down to 50 nΦ_0 Hz$^{-1/2}$, spin noise of 0.5 μ_B Hz$^{-1/2}$ and field noise down to 30 nT Hz$^{-1/2}$. Here, $\Phi_0 = h/2e$ is the two-electron flux quantum.

Tuning fork. For height control we attached the SOT to a quartz tuning fork as described in ref. [40]. The tuning fork was electrically excited at a resonance frequency of ~33 kHz. The current through it was amplified using a home-built trans-impedance amplifier, designed based on ref. [44] and measured using a lock-in amplifier. The scanning was performed at a constant height of 20–50 nm above the surface of the top hBN. The tuning fork was vibrated along the $\hat{x}$ direction, causing the SOT to vibrate with it with a controllable amplitude x_{ac} in the range of 20–100 nm r.m.s. In addition to the height control, we exploited the SOT vibration to acquire the spatial derivative of the local B_z field, $B_z^{TF} = x_{ac} \partial B_z / \partial x$, using a lock-in amplifier as described below.

Modulation techniques. To avoid the $1/f$ noise of the SOT that is present at frequencies below ~1 kHz, we acquired a.c. signals due to two types of modulation instead of measuring the local d.c. $B_z(x, y)$.

Backgate modulation B_z^{ac}. We applied a small a.c. excitation to the backgate (Fig. 4a), $V_{bg} = V_{bg}^{dc} + V_{bg}^{ac} \cos(2\pi f t)$, where $f \approx 5$ kHz. The corresponding $B_z^{ac} = V_{bg}^{ac} \partial B_z / \partial V_{bg}$ was then measured by the SOT using a lock-in amplifier.

Spatial modulation B_z^{TF} allowing direct current imaging. The advantage of the tuning fork-induced spatial modulation of the SOT position x_{ac} is that it provides a convenient means for direct imaging of the $\hat{y}$ component of the local current density $J_y(x)$. Consider a current element J_y flowing in a long and narrow strip of width Δx carrying a total current $I_y = \Delta x J_y$ in the $-\hat{y}$ direction (Supplementary Fig. 3a). The magnetic field $B_z(x)$ generated by the current and measured at height h above the current plane is described by the Biot–Savart law. For heights $h > \Delta x$, $B_z(x)$ is essentially governed only by the total current I_y in the strip, independent of Δx (Supplementary Fig. 3b). The $B_z(x)$ is an antisymmetric function with a steep slope above the current strip. The spatial derivative $\partial B_z / \partial x$ has a sharp peak at the strip location with a height proportional to I_y and a width determined by the scanning height h (Supplementary Fig. 3c).

Measuring $B_z^{TF} = x_{ac} \partial B_z / \partial x$ thus provides a convenient method for direct visualization of the spatial current distribution $J_y(x)$ with a resolution limited by the scanning height and the SOT diameter, as demonstrated by the simulation of three counterpropagating current strips in Supplementary Fig. 3d–f.

Electrostatically defined QH edge states. Using the experimental set-up of Fig. 3a, setting $\nu_L = 0$ and varying ν_R, we can create the situation of electrostatically defined edge states. Supplementary Fig. 7 and Supplementary Video 2 show the evolution of J^T and J^{NT} edge currents versus ν_R. Several recent studies have shown evidence of charge accumulation along the physical edges of graphene upon changing the carrier concentration with the backgate[27,34,45–48]. This charge accumulation apparently leads to complicated configurations of QH edge states and unconventional transport and dissipation[27,34]. An important finding here is that no such charge accumulation occurs in the case of our electrostatically defined edge. This is evidenced in Supplementary Fig. 7f by the monotonic upward bending of LLs visualized by the bright traces of the incompressible strips. In the case of charge accumulation at the edge, the LLs should have a non-monotonic behaviour with downward bending before the upturn towards the edge. We postulate that this absence of charge accumulation plays a central role in the improvement of the fractional QH effect in electrostatically defined devices[49].

We now focus on the microscopic details of the QH edge evolution upon varying ν_R. Similar to the case of a p–n junction, a strip of J^T appears when reaching $\nu_R = 2$ (Supplementary Fig. 7c) and moves towards the gate-defined edge as ν_R is increased (Supplementary Video 2). It is followed by a counterpropagating J^{NT} that increases with ν_R (Supplementary Fig. 7d). This sequence of advancing J^T and J^{NT} pairs repeats itself (Supplementary Fig. 7e) upon filling of every following LL, as clearly seen in Supplementary Fig. 7f. Note that every pair of full-valued J^{NT} and J^T for $|n| \geq 1$ carries almost no net current (Supplementary Fig. 5). As a result, when the edge states become too dense we can no longer resolve them within our spatial resolution.

Supplementary Fig. 7g shows a simplified schematic diagram of the QH edge states[26]. Each edge state carries a pair of counterpropagating currents[4]: J^{NT} flowing upstream in the outer compressible strip of the edge state and J^T flowing downstream with the edge chirality along the inner incompressible region. Let us focus on the $n = 2$ QH edge state. Supplementary Fig. 7g depicts the situation in which the Fermi level ε_F is just below $n = 3$ LL. In this case the integrated currents are maximal, I_{max}^{NT} and I_{max}^T, and because their magnitudes are comparable (Supplementary Fig. 5) the overall current flowing in the edge state is close to zero. J^{NT} arises from the fact that in the incompressible strip the carrier density in the $n = 2$ LL decreases from a fully occupied to an empty level. J^T, in contrast, is caused by the potential difference across the incompressible region, which drives the current in all of the three underlying occupied LLs. On decreasing ε_F within the gap, I^T decreases while I^{NT} remains unchanged. Because I^T is proportional to $\varepsilon_F - \varepsilon_n$, where ε_n is the energy of the highest underlying occupied LL, measurement of the local I^T thus provides direct information on the local value of the electrochemical potential, which becomes essential under non-equilibrium conditions, as discussed in the following. When ε_F reaches just above the $n = 2$ LL, the downstream I^T in this QH edge state vanishes and only the upstream I^{NT} remains (Supplementary Fig. 7h). In this situation the total equilibrium current carried by the $n = 2$ QH edge state reaches its maximum value given by the upstream I_{max}^{NT}. Decreasing ν_R further will start depleting the $n = 2$ LL, correspondingly reducing I^{NT} until it vanishes upon the full depletion of the $n = 2$ LL. Similarly to I^T, such local measurement of I^{NT} thus provides key information on the occupation level of the LL in a non-equilibrium case. The above process will then repeat itself for the $n = 1$ QH edge state. The net equilibrium current in the QH edge states thus oscillates periodically with V_{bg}. Note that the $n = 0$ QH edge state in graphene is an exception as it carries only I^T while $I^{NT} = 0$. This absence of I^{NT} in the $n = 0$ LL is clearly seen in Supplementary Fig. 7f and Supplementary Video 2. This is not the case for a 2D electron gas of massive particles, for example in GaAs heterostructures, where all the LLs carry pairs of counterpropagating I^{NT} and I^T (Supplementary Fig. 5).

One may ask what happens to the currents flowing along the artificial edge (Fig. 3c–e and Supplementary Fig. 7c–e) as they approach the physical sample edges, without violating charge conservation. J^T and J^{NT} follow equi-potential V and equi-density n_e lines, respectively. Both V and n_e are continuous manifolds that bend towards the sample edges. It is therefore expected that all the equilibrium currents form closed counterpropagating loops following the physical and artificial edges. Another possibility, however, is that steep potential and carrier density gradients, on a scale smaller than the magnetic length l_B, or strong disorder that locally destroys the QH state, may cause J^T and J^{NT} to essentially disappear at some point in the sample. Considering J^T and J^{NT} separately, this may seem to violate charge conservation. However, considering them together, the charge conservation is restored because the current flowing in one of them is returned through the counterflowing path of the other. This situation apparently occurs in magic angle twisted bilayer graphene[32].

The above description of counterpropagating currents that change their relative magnitude as a function of local electrochemical potential and carrier density, provides an important framework for exploring non-equilibrium phenomena. In the equilibrium case the total current integrated over the width of the sample must be zero for I^T and for I^{NT} separately. In out-of-equilibrium

conditions in the presence of external bias, the total I^{NT} should still remain zero, because it is proportional to the difference in the carrier densities at the opposite edges of the sample, but the density at the sample edges always has to vanish. The total I^T, in contrast, becomes finite due to the induced transverse net drop in the electrochemical potential. This information provided by global transport measurements, however, does not reveal the local microscopic out-of-equilibrium processes. Under out-of-equilibrium conditions, each QH edge state generally has a different, position-dependent electrochemical potential and non-equilibrium carrier distribution driven by external voltage bias or by other external perturbations including thermal gradients and heat flow. The equilibration process due to electron–electron scattering within each state and between neighbouring edge states is a subject of extensive studies using spectroscopic transport measurements[50-52]. These measurements, however, provide information only at specific lithographically predefined locations. In addition, contacts may affect the current flow, making these measurements invasive. Because the local electrochemical potential and the carrier density determine the relative magnitude and distribution of J^T and J^{NT} within each individual edge state, our technique may thus provide a unique imaging tool to visualize and explore non-equilibrium phenomena and the microscopic mechanisms of equilibration, edge reconstruction, and charge and heat transfer between individual QH edge states under various out-of-equilibrium conditions. This will be the subject of future work.

TME response to a point charge. We show that a point electric charge Q_e placed at height z_0 above a topological surface characterized by a quantized Hall conductance σ_{yx} induces a magnetic field above the surface identical to that of a magnetic monopole of charge Q'_m placed at height z_0 below the surface. In the incompressible QH state the electric field $\mathbf{E}$ produced by the charge Q_e is unscreened and its radial component E_r along the topological surface is given in cylindrical coordinates by

$$E_r(r) = \frac{Q_e}{4\pi\epsilon_0} \frac{r}{(r^2 + z_0^2)^{3/2}}$$

leading to a circulating topological current density $J^T_\varphi(r) = \sigma_{yx} E_r(r)$. The magnetic field along the z axis is then obtained by integrating the Biot–Savart relation for concentric current rings with current $dI(r) = J_\varphi(r)dr = \sigma_{yx}E_r(r)dr$:

$$B_z(z) = \int_0^\infty \frac{\mu_0}{4\pi} \frac{2\pi r^2}{(r^2+z^2)^{3/2}} \frac{\sigma_{yx}Q_e}{4\pi\epsilon_0} \frac{r}{(r^2+z_0^2)^{3/2}} dr = \frac{\mu_0}{4\pi} \frac{Q'_m}{(|z|+|z_0|)^2}$$

Here, $Q'_m = \sigma_{yx}Q_e/2\epsilon_0$. Using $\sigma_{yx} = Ce^2/h$ we obtain

$$Q'_m = \frac{1}{2\epsilon_0} \frac{Ce^2}{h} Q_e = C\alpha c Q_e$$

where α is the fine structure constant, c is the speed of light and C is the Chern number. Note that Q'_m flips sign with B_z. In the calculations above, we took B_z in the positive $\hat{z}$ direction.

Monopole fragility. To induce a magnetic monopole, the entire sample has to be in the incompressible state. Hence, the potential variation across the sample cannot exceed the energy gap $\Delta E_n/e$. Due to its low density of states and the linear dispersion, graphene possesses a much larger QH energy gap than any other known time-reversal-symmetry-broken topological system. For an applied magnetic field of $B = 1$ T, $\Delta E_1 = 36.3$ meV ≈ 420 K. Even for such a large gap, a single electron charge trapped on the surface of hBN or located on the scanning tip is sufficient to destroy the monopole state, as demonstrated numerically in Supplementary Fig. 8. In this case, an incompressible state throughout the sample that is required for inducing a magnetic monopole cannot be formed at any value of V_{bg}. In magnetic topological insulators the energy gap is estimated to be of the order of 0.5 K (refs. [53-55]), and hence native charge disorder as low as $1 \times 10^{-3} e$ is sufficient to prevent the formation of a magnetic monopole. Because magnetically doped topological insulators are found to be highly disordered[43,56], we conclude that the proposed observation of the induced magnetic monopole in them[2] is unfeasible at present.

Semiclassical numerical simulations. COMSOL simulations were used for solving the electrostatic equations for the potential V and charge density $\rho = -en_e$ in graphene. The simulations included one or two metallic backgates, graphene, and the SOT acting as a metallic local top gate (Supplementary Fig. 10) in a $2 \times 2 \times 2\,\mu m^3$ volume with boundary conditions of $E_\perp = 0$ on the box surfaces and a constant electric potential on the backgate and SOT surfaces. We performed an iterative self-consistent solution for $V(x,y,z)$ as follows.

Step 1: $V(x,y,z)$ was calculated by solving $\nabla \cdot \mathbf{E} = \rho/\epsilon_r\epsilon_0$ and $\mathbf{E} = -\nabla V$ with given V_{bg}, V_{tg} and an initial charge distribution $\rho(x,y) = \rho_0$ on graphene, where ϵ_r is the relative permittivity of the material (we took $\epsilon_r = 4$ for hBN and 3.9 for SiO$_2$) and ϵ_0 is the permittivity of vacuum.

Step 2: The solution for $V(x,y,z=0)$ was used as an input to a smoothed LL occupation function $\nu(V)$ (Supplementary Fig. 10d) defining the local charge density on the graphene, $\rho(x,y) = eB\nu(V)/\phi_0$. The resulting $\rho(x,y)$ was then used as an input to step 1.

These steps were repeated until a self-consistent solution was attained. Once $V(x,y,z=0)$ and $\rho(x,y)$ were found, the topological and non-topological surface currents in graphene were calculated using $\mathbf{J}^T = -\sigma\nabla V$ and $\mathbf{J}^{NT} = \frac{\mu_e^{(n)}}{e}\nabla \times |\rho| \hat{z}$, where $\sigma_{xy}(x,y) = -\sigma_{yx}(x,y) = -\nu(x,y)e^2/h$ and $\sigma_{xx} = \sigma_{yy} = 0$ are the components of the conductivity tensor σ. The total current distribution $\mathbf{J}^{tot} = \mathbf{J}^T + \mathbf{J}^{NT}$ was then used to derive the induced magnetic field $B_z(x,y,z)$ through the Bio–Savart relation.

Measurement and simulation parameters. Figure 2b–d simulation: $B = 1.435$ T, Si backgate distance from graphene 252 nm, bottom hBN thickness 37 nm, top hBN thickness 15 nm. Other parameters are included in the figure caption.

Figure 2j simulation: Same as for Fig. 2b–d and with SOT diameter 60 nm, scan height 35 nm (50 nm above graphene) and $x_{ac} = 35$ nm (r.m.s.).

Figure 2h: Device A, $B = 1.03$ T, SOT diameter 55 nm, scan height 70 nm, $x_{ac} = 130$ nm (r.m.s.), pixel size 55 nm, 100 ms per pixel.

Figure 2i: Device A, $B = 1.05$ T, SOT diameter 55 nm, scan height 60 nm, $x_{ac} = 90$ nm (r.m.s.), pixel size 95 nm, 60 ms per pixel.

Figure 3b–e and Supplementary Video 1: Device B, $B = 1.06$ T, SOT diameter 50 nm, scan height 30 nm, $x_{ac} = 35$ nm (r.m.s.), pixel size 18 nm, 80 ms per pixel.

Figure 3f: Device B, $B = 1.06$ T, SOT diameter 50 nm, scan height 25 nm, $x_{ac} = 35$ nm (r.m.s.), pixel size 13 nm, 80 ms per pixel.

Figure 3g–j simulation: $B = 1.45$ T, SOT height 30 nm (32 nm above graphene), $x_{ac} = 35$ nm (r.m.s.), Si backgate distance from graphene 250 nm, graphite backgate distance from graphene 35 nm, top hBN thickness 2 nm.

Figure 4a,b simulation: $B = 1.415$ T, bottom hBN thickness 17 nm, SiO$_2$ thickness 218 nm, top hBN thickness 15 nm, SOT height 30 nm (45 nm above graphene), backgate excitation (Fig. 4b) $V_{bg}^{ac} = 50$ mV (r.m.s.).

Figure 4i: Device A, $B = 1.03$ T, SOT diameter 55 nm, scan height 30 nm, backgate excitation $V_{bg}^{ac} = 70$ mV$_p$ square wave at 5.15 kHz, 100 ms per point.

Supplementary Fig. 6: Device B, $B = 1.06$ T, SOT diameter 50 nm, scan height 40 nm, $x_{ac} = 30$ nm (r.m.s.), pixel size 30 nm, 60 ms per pixel.

Supplementary Fig. 7b–e and Supplementary Video 2: Device C, $B = 0.94$ T, SOT diameter 69 nm, scan height 30 nm, $x_{ac} = 25$ nm (r.m.s.), pixel size 20 nm, 80 ms per pixel.

Supplementary Fig. 7f: Device C, $B = 0.94$ T, SOT diameter 69 nm, scan height 30 nm, $x_{ac} = 55$ nm (r.m.s.), pixel size 10 nm, 60 ms per pixel.

Data availability

The data represented in Figs. 2b–d,h–j, 3b–j and 4b–i are available with the online version of this paper. All other data that support the plots within this paper and other findings of this study are available from the corresponding author upon reasonable request.

References

35. Kim, Y. et al. Even denominator fractional quantum Hall states in higher Landau levels of graphene. *Nat. Phys.* **15**, 154–158 (2019).
36. Masubuchi, S. et al. Autonomous robotic searching and assembly of two-dimensional crystals to build van der Waals superlattices. *Nat. Commun.* **9**, 1413 (2018).
37. Kim, Y. et al. Charge inversion and topological phase transition at a twist angle induced van Hove singularity of bilayer graphene. *Nano Lett.* **16**, 5053–5059 (2016).
38. Goossens, A. M. et al. Mechanical cleaning of graphene. *Appl. Phys. Lett.* **100**, 073110 (2012).
39. Lindvall, N., Kalabukhov, A. & Yurgens, A. Cleaning graphene using atomic force microscope. *J. Appl. Phys.* **111**, 064904 (2012).
40. Halbertal, D. et al. Nanoscale thermal imaging of dissipation in quantum systems. *Nature* **539**, 407–410 (2016).
41. Halbertal, D. et al. Imaging resonant dissipation from individual atomic defects in graphene. *Science* **358**, 1303–1306 (2017).
42. Finkler, A. et al. Scanning superconducting quantum interference device on a tip for magnetic imaging of nanoscale phenomena. *Rev. Sci. Instrum.* **83**, 073702 (2012).
43. Lachman, E. O. et al. Visualization of superparamagnetic dynamics in magnetic topological insulators. *Sci. Adv.* **1**, e1500740 (2015).
44. Kleinbaum, E. & Csáthy, G. A. Note: a transimpedance amplifier for remotely located quartz tuning forks. *Rev. Sci. Instrum.* **83**, 126101 (2012).
45. Silvestrov, P. G. & Efetov, K. B. Charge accumulation at the boundaries of a graphene strip induced by a gate voltage: electrostatic approach. *Phys. Rev. B* **77**, 155436 (2008).
46. Hettmansperger, H. et al. Quantum Hall effect in narrow graphene ribbons. *Phys. Rev. B* **86**, 195417 (2012).
47. Chae, J. et al. Enhanced carrier transport along edges of graphene devices. *Nano Lett.* **12**, 1839–1844 (2012).

48. Barraud, C. et al. Field effect in the quantum Hall regime of a high mobility graphene wire. *J. Appl. Phys.* **116**, 073705 (2014).

49. Chen, S. et al. Competing fractional quantum Hall and electron solid phases in graphene. *Phys. Rev. Lett.* **122**, 026802 (2019).

50. Itoh, K. et al. Signatures of a nonthermal metastable state in copropagating quantum Hall edge channels. *Phys. Rev. Lett.* **120**, 197701 (2018).

51. Venkatachalam, V., Hart, S., Pfeiffer, L., West, K. & Yacoby, A. Local thermometry of neutral modes on the quantum Hall edge. *Nat. Phys.* **8**, 676–681 (2012).

52. Altimiras, C. et al. Tuning energy relaxation along quantum Hall channels. *Phys. Rev. Lett.* **105**, 226804 (2010).

53. Chang, C.-Z. et al. Zero-field dissipationless chiral edge transport and the nature of dissipation in the quantum anomalous Hall state. *Phys. Rev. Lett.* **115**, 057206 (2015).

54. Liu, M. et al. Large discrete jumps observed in the transition between Chern states in a ferromagnetic topological insulator. *Sci. Adv.* **2**, e1600167 (2016).

55. Fox, E. J. et al. Part-per-million quantization and current-induced breakdown of the quantum anomalous Hall effect. *Phys. Rev. B* **98**, 075145 (2018).

56. Lachman, E. O. et al. Observation of superparamagnetism in coexistence with quantum anomalous Hall $C = \pm 1$ and $C = 0$ Chern states. *npj Quantum Mater.* **2**, 70 (2017).

Acknowledgements

Author contributions

A.U. and E.Z. designed the experiment. A.U. and S.G. performed the measurements and the data analysis. Y.K. and J.S. designed and fabricated the samples. K.B. fabricated the SOTs. C.K.L. performed the quantum mechanical calculations and contributed to the theoretical analysis. N.A. performed the Comsol simulations and contributed to the theoretical analysis. E.O.L. designed and built the scanning SOT microscope. Y.M. fabricated the tuning forks. T.T. and K.W. grew the hBN crystals. A.U., S.G. and E.Z. wrote the manuscript with input from J.S. and Y.K. All authors participated in discussions and in writing the manuscript.

Competing interests

The authors declare no competing interests.

Additional information

Supplementary information is available for this paper at https://doi.org/10.1038/s41567-019-0713-3.

Correspondence and requests for materials should be addressed to A.U. or E.Z.

Reprints and permissions information is available at www.nature.com/reprints.